ELSEVIER

Earth and Planetary Science Letters 157 (1998) 57–67

EPSL

Global de-correlation of the topography of transition zone discontinuities

Yu Gu *, Adam M. Dziewonski, Carl B. Agee

Department of Earth and Planetary Sciences, Harvard University, Cambridge, MA 02138, USA

Received 23 September 1997; revised version received 23 January 1998; accepted 30 January 1998

Abstract

Analysis of long-period shear-wave underside reflections from upper mantle discontinuities shows the shape of the 410 km discontinuity to be neither globally nor locally correlated with that of the 660-km discontinuity. The long wavelength pattern of *410* topography is dominated by degree-1 spherical harmonics and has a reasonable correlation with the seismic velocity perturbations in the mantle above it. The global topography of *660*, dominated by degree-2 spherical harmonics, is strongly correlated with shear-wave velocity variations in the transition zone. The poor correlation between the observed topography of the 410- and 660-km discontinuities is inconsistent with a simple model of large scale, whole mantle flow, thus implying a more complex pattern, which includes at least temporary accumulation of subducted material in the transition zone [Ringwood and Irifune, Nature 331 (1988) 131–136; Tackley et al., Nature 361 (1993) 699–704]. The modest seismic discontinuity at 520 km is well observed when the reflections are under mid-age oceans, but is not observed when they are under continental shields. Interpretation of this observation in terms of olivine depletion in the deep continental mantle indicates the possible existence of continent–ocean chemical heterogeneity at depths exceeding 500 km.

Keywords: topography; transition zones; discontinuities; velocity structure; tomography

1. Introduction

The question of the depth to which continent–ocean differences persist is important to understanding the patterns of flow in the mantle, and has implications for the geochemistry and mineralogy of the mantle and its formation and evolution. Global seismic tomography [1–4], with resolution of 1000–2000 km, reveals correlations of long wavelength velocity perturbations with the surface tectonics to depths as great as 250–300 km, and perhaps deeper. The amplitude of anomalies below 250–300 km depth is relatively low in comparison with those near the surface, and the details revealed by tomography strongly depend on the modeling strategy. Reflected waves provide an effective method of mapping upper mantle discontinuities, as their travel times offer an order of magnitude greater sensitivity for resolving these discontinuities than do refracted waves.

With the limited resolution of the structure on both sides of a discontinuity achievable in seismic tomography based on transmitted waves [5], studies of topography of the transition zone seismic discontinuities using reflected waves offer potentially new information about the past and on-going physical and chemical processes in the mantle. Developments in

* Corresponding author. E-mail: gu@eps.harvard.edu

0012-821X/98/$19.00
PII S0012-821X(98)00027-2

the detection of secondary phases, such as ScS reverberations [6,7], P-to-S and S-to-P converted waves [8,9] and underside reflections from mantle discontinuities (SS precursors) [10–16], have improved our ability to determine lateral variations in the depth of these discontinuities. Of the phases listed above, SS precursors are particularly useful for global mapping, since the mid-path reflection point can be located far from a source or a station and, therefore, provide coverage that is not strictly limited by the distribution of earthquakes and receivers. SS precursor data have been used by Shearer and Masters [17] to derive the first global map of the 660-km discontinuity and by Shearer [12] to map the 410- and 660-km discontinuities (hereafter, we shall refer to the discontinuities by their depth: *410*, *660*, etc.).

Some questions, such as the geodynamic significance of the topography of *410* and its relation to *660* remain, however, unclear. Also, the existence [18,19] and global occurrence [14] of the 520-km discontinuity [10,13,20] (*520*) have been questioned. The rapid increase in the number and quality of stations of the global seismographic network in recent years, as well as some improvements in data processing, motivated us to undertake a new global study using a significantly larger data base than that available to previous studies.

2. Data selection and processing

We examine the travel times and amplitudes of SS precursors using high-quality broad-band and long-period transverse component seismograms. We restrict our data set to shallow events of depth less than or equal to 75 km. This restriction reduces complications due to depth phases and helps to produce more consistent stacking results by more or less equalizing the source. The epicentral distance between source and receiver is restricted to lie between 100 and 160°.

The size of our data set – 13,000 seismograms (11,000 after interactive evaluation) – compares favorably with those used in other studies: 3139 in Shearer and Masters [17], 5884 in Shearer [12] and 3100 in Gossler and Kind [14]; the data set of Flanagan and Shearer [15,16] is comparable to that used here. The mid-path reflection points are shown in Fig. 1a. The coverage is particularly dense in the Northern Pacific Ocean and the Indian Ocean, and relatively sparse in parts of South America and the Southern Atlantic Ocean.

We use the phase equalization (stacking) method to increase signal-to-noise ratio. The instrument response is deconvolved from each observed seismogram prior to further processing. After rotation of the three-component seismograms, we apply a half-Welch filter to the SH component seismograms with cut-off periods at 15 and 100 s. Experimentation with different filters indicates that use of this filter gives robust stacking results. Since stacking results strongly depend on the quality of each individual trace, noise with abnormally large amplitude can contaminate the entire stack. Thus we adopt a crude signal-to-noise ratio cut-off as an additional constraint on the data set. We calculate peak absolute amplitude within a 1-min time window around the predicted arrival time of SS, and use this as our peak signal amplitude. The peak absolute amplitude within a time window of 5 min, ending 50 s prior to the SS arrival, is used as the peak noise amplitude. Any record with an S/N ratio smaller than 3 is discarded.

The individual seismograms are binned using 10° spherical caps. We divide the Earth's surface into a network of grid points roughly 10° arc distance

Fig. 1. (a) Reflection points (13,087) of SS precursors prior to interactive processing. (b) Topography map of *410*. Cap averaged depth residuals are plotted as triangles. The red triangles represent positive elevations of the *410* boundary with respect to the global mean depth of 411 ± 2 km; the blue triangles represent depression of the boundary. The cap-averaged depth residuals are fit using a spherical harmonic expansion up to degree-12, shown by color contours. (c) Shear-wave velocity perturbation at 350 km depth; the Earth model is S12_WM13 [1], a degree-12 global model of lateral heterogeneity for the S-velocity. (d) Topography map of *660*. The definition of the symbols is the same as in (b), and the depth residuals are relative to the global mean of 654 ± 2 km. (e) Shear-wave velocity perturbation in the transition zone at 550-km depth for the same model as in (c). (f) Cap-averaged transition zone thickness. The red triangles represent thinner transition zones relative to the global mean thickness of 243 km; the blue triangles represent thicker transition zones. The cap-averaged thickness residuals are fit using a spherical harmonic expansion up to degree-12, shown by color contours.

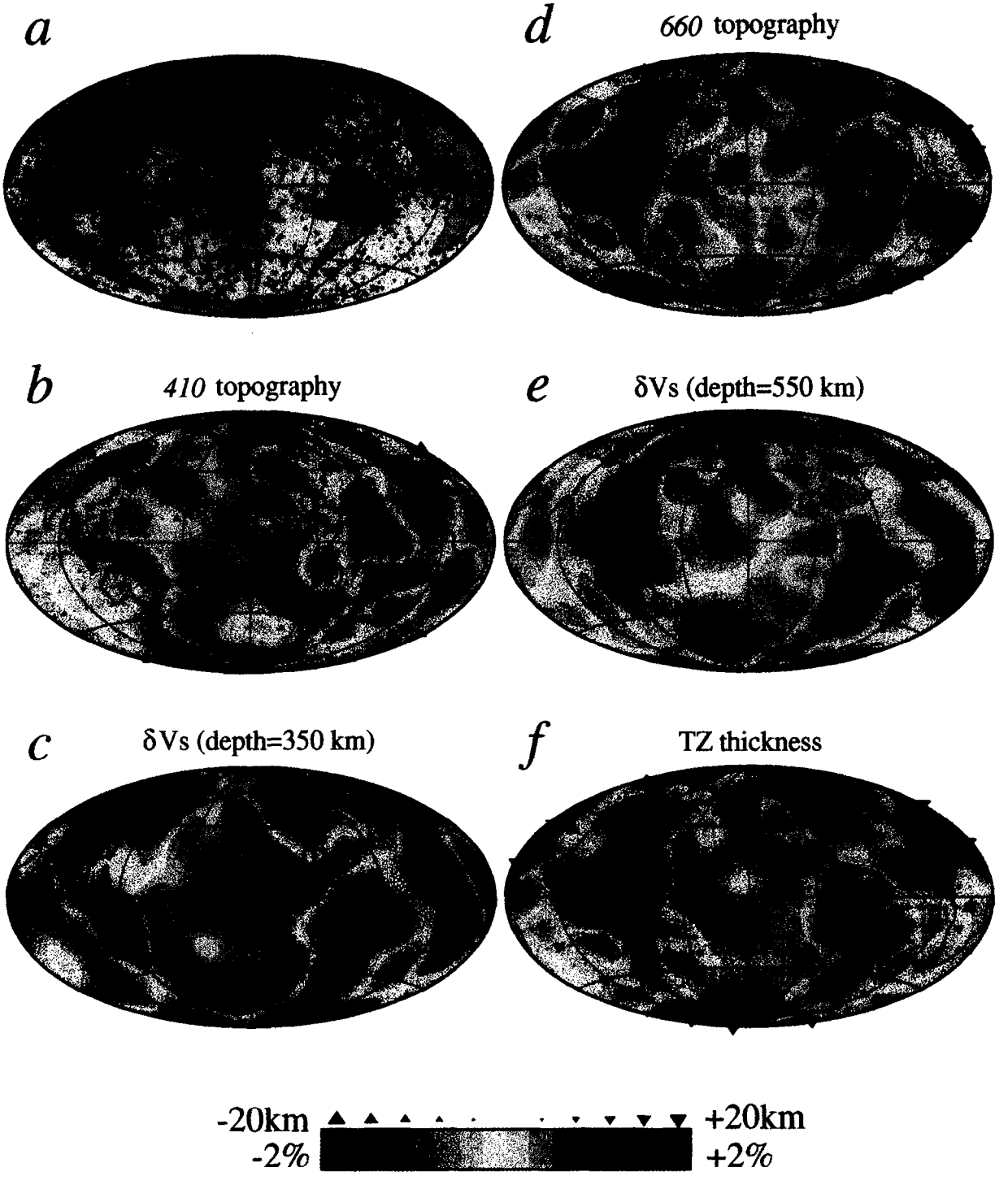
a
d
660 topography
b
410 topography
e
δVs (depth=550 km)
c
δVs (depth=350 km)
f
TZ thickness
-20km
+20km
-2%
+2%

apart; there are 412 such points. All seismograms with surface reflections within a 10° circle around a grid point are included in building the stack; a minimum of 10 records is required for a measurement to be reported for a particular grid point. Our 10°-radius bins are similar to those used in [10] and [12], but are significantly smaller than those used in [14]. This averaging algorithm implies light smoothing: there is an overlap in the data used to derive stacks for adjacent points, but it is relatively small. The equivalent low-pass filter is all-pass to the degree-9 spherical harmonic and the response decreases mildly after that.

Prior to stacking, both observed and synthetic seismograms are aligned on the first major swing of the SS phase using cross-correlation. This procedure corrects for source and station effects. The seismograms are then manually edited; the polarity is reversed if necessary. The maximum amplitude of the SS phase, the S/N ratio and the maximum amplitude within the precursor window are saved for the normalization and weighting of the seismograms.

The observed travel times of S660S, S410S and S220S are corrected individually to a reference distance of 130° using travel time tables which were calculated for PREM [21]. The seismograms (both observed and synthetic) are then shifted accordingly. This procedure allows us to obtain a coherent stacking result using records with different epicentral distances. Before stacking, we apply time shifts (in the spectral domain, using FFTs) for each phase in each synthetic seismogram, to correct for crust (continent–ocean function), free surface topography at the reflection point. Corrections for laterally varying velocities are calculated using 3-D ray tracing [22] for model S12_WM13 [1]; occasionally, the 'true' reflection point can be found as far as 5° away from that predicted by the radially symmetric reference model. These corrections allow us to isolate the effect of topography changes on the differential travel time of SS–SdS. Then each seismogram is normalized by its peak amplitude in the precursor window to correct for the effect of earthquake magnitude, and weighed by the square root of S/N to give higher weighting to the best quality seismograms. After this procedure, we stack the seismograms and measure the travel time residuals between the stacked data and synthetic seismograms.

The travel time perturbation due to boundary undulation for a reflected wave can be approximated by the following expression:

$$\delta t = -\frac{2\delta(r)}{r}(\eta^2 - p^2)^{\frac{1}{2}}$$

where $\eta = r/v(r)$ and p is the ray parameter [23]. Given the differential travel time perturbations δt, we can calculate the perturbation δr to the discontinuity radius. The effect of varying takeoff angles for different distances is incorporated by varying the ray parameter values.

Since the measurements are made by combining many reflection seismograms together, it is useful to examine the theoretical resolving power of these reflected phases. One way to do so is to estimate the size of the Fresnel zone. In our case, the Fresnel zone refers to the frequency dependent area on the Earth's surface, or upper mantle discontinuity surfaces, which influences the bounce point of SS or its precursors. The resulting Fresnel zone from 3-D ray tracing [22] is a minimax pattern with an approximate width of 10°, comparable to the radius of the caps we use to bin the data. Similar results are found in Ref. [12]. The average standard error in our measured depths is 2–3 km, inferred from the bootstrapping method, though few of the cap values in the southern hemisphere have uncertainties up to 12–15 km.

3. Topography of the 410- and 660-km discontinuities

Fig. 1b shows the topography map for *410* based on the differential travel time measurements of SS–S410S. Each symbol represents the measured depth perturbation from the average of 411 km at the corresponding cap location. The depth perturbations are determined at 380 caps out of 412 possible. Using a damped least-squares inversion, we fit the values of spherical harmonics up to degree 12; the synthesis of the spherical harmonic expansion is shown by color contours. The map shows a long-wavelength depression of the boundary under most parts of the Pacific and Indian Oceans. Positive elevations are seen under continental regions such as Eurasia, North America, Australia, Antarctica and parts of Africa.

Fig. 1d shows the result of topography measurements for *660*; the average of 370 cap values is 654 km; the contours are obtained in the same way as in Fig. 1b. The most notable features are the large depression of the boundary under the western Pacific, Tonga and South America. Considering data coverage (Fig. 1a), the depression under the western Pacific extending from Kamchatka to the Philippines is the most robust of the long wavelength features. The depth perturbations from the global mean are as large as 25 km; this result is consistent with earlier work, and its cause has been associated with the effect of subduction [10,24]. No significant features are evident near the ridges, for example the East Pacific Rise.

In Fig. 2a we compare the depth perturbations to *410* with those to *660*, when both values are available for the same cap. There is no significant correlation, though we would expect a negative correlation if both discontinuities were influenced by temperature anomalies of the same sign, such as those which would be induced by a vertical upward or downward adiabatic flow in an isochemical olivine-rich mantle. The lack of correlation indicates that the deformation of the two discontinuities is likely caused by different processes in the mantle.

We next examine the power spectra of the two topographies, in order to investigate the possibility that they may be dominated by particular wavelengths, such as those found in the spectra of lateral heterogeneities [25,26]. The power spectrum of the spherical harmonic coefficients for *410* has a strong degree-1 signature (Fig. 2b) and little power in degree-2; the square symbols show results obtained using the data of Shearer [12]. Though the rms amplitude of the latter data is higher by some 20%, the pattern is very similar. There is a reasonable correlation in the topography of *410* (Fig. 1b) and the seismic velocity variations right above the transition zone (Fig. 1c): to the first order, *410* is depressed under most parts of the Pacific ocean and elevated under major continents. If this discontinuity represents the phase change from α-olivine to β-phase, then the difference in *410* topography under continents and the largest ocean on Earth may reflect the thermal difference between these regions. If we assume the slope of the phase boundary from Fo90 composition [27], the average difference in depth of approximately 5 km corresponds to a difference in temperature of 70°C; this could be consistent with the hypothesis of deep continental roots [28,29]. There are exceptions to this observation, however, on a local scale, which maybe an effect caused by measurement errors, presence of chemical heterogeneities, or smaller scale thermal anomalies. Also, the most distinct anomaly is observed under the Pacific, where it could be associated with the vigorous oceanic spreading.

Unlike the topography of *410*, the power spectrum of *660* topography (Fig. 2c) is dominated by degree-2, with degree-1 being relatively small; the same is true for the results of Shearer [12]. Because shear velocity perturbations in the transition zone also have a strong degree-2 signature [25,26], we compare in Fig. 1e the shear-wave velocity map of model S12_WM13 [1] at 550 km depth (middle of the transition zone) to our *660* topography in Fig. 1d. There is an excellent correlation between the velocity perturbations and *660* topography. In regions where large positive velocity anomalies are found, such as subduction zones in the western Pacific and South America, we also find significant depression of the 660-km boundary; this is similar to the conclusions of Shearer and Masters [17]. Thus, at depths close to 660 km, the effect of the accumulated material becomes more important than the thermal differences between the continental and oceanic structures, which may be influencing the depth of *410*.

4. Thickness of the transition zone and 520-km discontinuity

The thickness of the transition zone (Fig. 1f) based on individual measurements of the depth to *410* and *660* reveals some continent–ocean difference; the transition zone is generally thinner under the oceanic regions, most notably the Pacific, and is thicker under continents, relative to the global average of 243 km. This would be consistent with the findings of Gossler and Kind [14], except for regions under major subduction zones where the transition zone is considerably thickened. The spectrum in Fig. 2d shows the combined effect of the topography of *410* and *660*, as degree-1 and -2 dom-

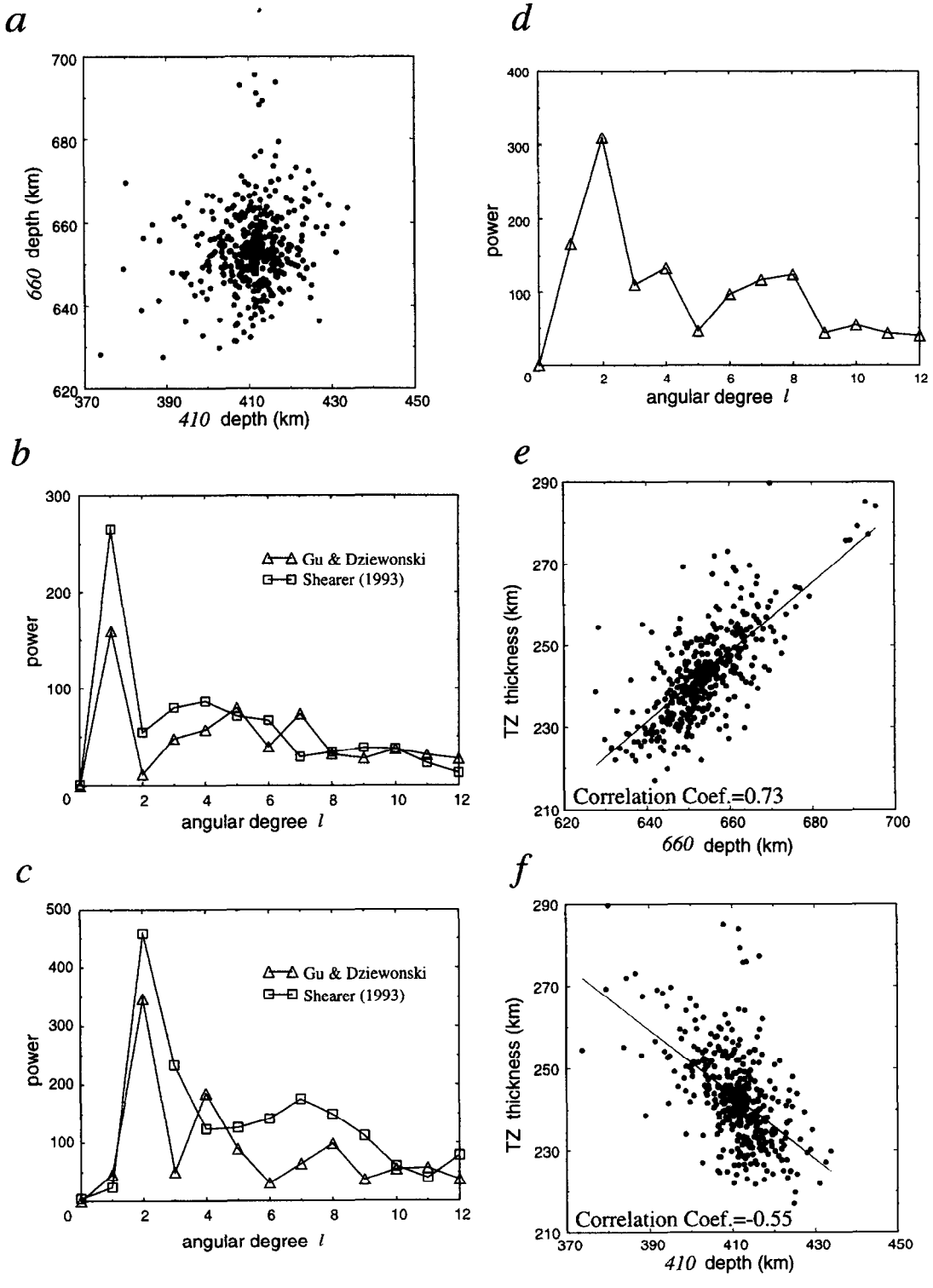
a
700
680
660
640
620
370
390
410
430
450
660 depth (km)
410 depth (km)
d
400
300
200
100
0
2
4
6
8
10
12
power
angular degree l
b
300
200
100
0
power
Gu & Dziewonski
Shearer (1993)
angular degree l
e
290
270
250
230
210
620
640
660
680
700
TZ thickness (km)
Correlation Coef.=0.73
660 depth (km)
c
500
400
300
200
100
power
Gu & Dziewonski
Shearer (1993)
angular degree l
f
290
270
250
230
210
370
390
410
430
450
TZ thickness (km)
Correlation Coef.=-0.55
410 depth (km)

inate the power spectrum of the map of the transition zone thickness. The strong influence of subduction, reflected in the power of degree-2, results mainly from the larger global topography of the 660-km discontinuity. The effects of discontinuity topography on transition zone thickness is evident in the TZ vs. discontinuity depth plots (Fig. 2e,f). The significantly higher absolute value of the correlation coefficient in Fig. 2f reflects the dominating effect of *660* topography on transition zone thickness.

There has been a debate over the existence of the 520-km discontinuity in the transition zone [10,13,14,18–20]; Gossler and Kind [14] proposed that it is not present everywhere. In an experiment designed to investigate a possible correspondence between the tectonic regime at the surface and the presence of, and possible variation in, the velocity contrast of the upper mantle discontinuities, we divide our surface reflection points according to the GTR1 regionalization of Jordan [30] and stack the data according to this model. The slowness stacks obtained from more than 1300 seismograms ($S/N \geq 3$) are shown in Fig. 3c,d; the results are consistent with those obtained from the best-quality data ($S/N \geq 5$). The most distinct results are obtained for the mid-age oceans and shields; the selected reflection points are shown in Fig. 3a. The synthetic and data slant–stacks contours are plotted in Fig. 3b–d; the representation is similar to that used by Gossler and Kind [14]. Fig. 3b is the stack of the synthetics calculated for PREM [21]; the arrivals of the underside reflections from the 670-, 400- and 220-km discontinuities present in the model are distinct. In the stacks of the mid-age ocean data (Fig. 3c), the arrivals of S410S and S660S are pronounced, but the S220S reflection, which should arrive nearly 80 s prior to SS, cannot be seen. The signal between S410S and S660S, not present in PREM [21], corresponds both in the arrival time and slowness to an underside reflection near 520 km. The peak amplitude of this phase is approximately 1–2% of that of SS, which is significantly larger than all other possible phases aside from S410S and S660S, reflecting a smaller acoustic impedance than those observed at *410* and *660*. Although the cause of this discontinuity is controversial, it has been proposed that it signals a phase transition from β-phase to γ-spinel in an olivine-rich mantle [32].

The shield data stacks (Fig. 3d), on the other hand, show no evidence for the presence of *520*; the signal between S660S and S410S arrivals is as flat as the synthetics in Fig. 3b – there is no *520* in PREM [21]. Although the shield data set is dominated by reflection points under the Canadian shield, the results are consistent with our separate regional stacks for the Canadian shield and African shield, indicating that the weak reflection from *520* is a real feature and not an artifact of data selection.

5. Discussion

Our observations, as shown above, indicate that the large-scale features of the *410* topography are correlated with the seismic velocity variations right above the transition zone, and *660* topography with the perturbations of the large wavelength shear-wave velocity in the transition zone. The effect of continental roots appears to influence the mantle structure to depths of at least 410 km. In contrast, the structure near the depth of 660 km is likely associated with the presence of the cold subducted material. Assuming that the velocity anomalies are proportional to temperature perturbations, this feature correlates with the negatively sloping phase boundary interval. The variation of the transition zone thickness is strongly

Fig. 2. (a) The depth correlation of *410* and *660* measured at each cap location; there is no significant correlation. (b) Comparison of the power spectra of degree-12 spherical harmonic expansion coefficients for *410* depth residuals estimated by Shearer [12] and by our study. Both results show a large degree-1 and a relatively small degree-2 signature. (c) Comparison of power spectra of degree-12 spherical harmonic expansion coefficients for *660* depth residuals estimated by Shearer [12] and by our study. Both results show a large degree-2, and a relatively small degree-1 signature. (d) Power spectra for the global transition zone thickness map. Both degree-1 and degree-2 are strong, reflecting the combined effect of the topography of *410* and *660*. (e) Correlation between the *410* topography and the transition zone thickness (labeled as *TZ*) at each cap location. The linear correlation coefficient is −0.55. (f) Same as (e), but for *660* topography. The absolute value of the linear correlation coefficient is 0.73; this is significantly higher than that of (e), indicating the dominating effect of the relatively larger *660* topography on the global transition zone thickness.

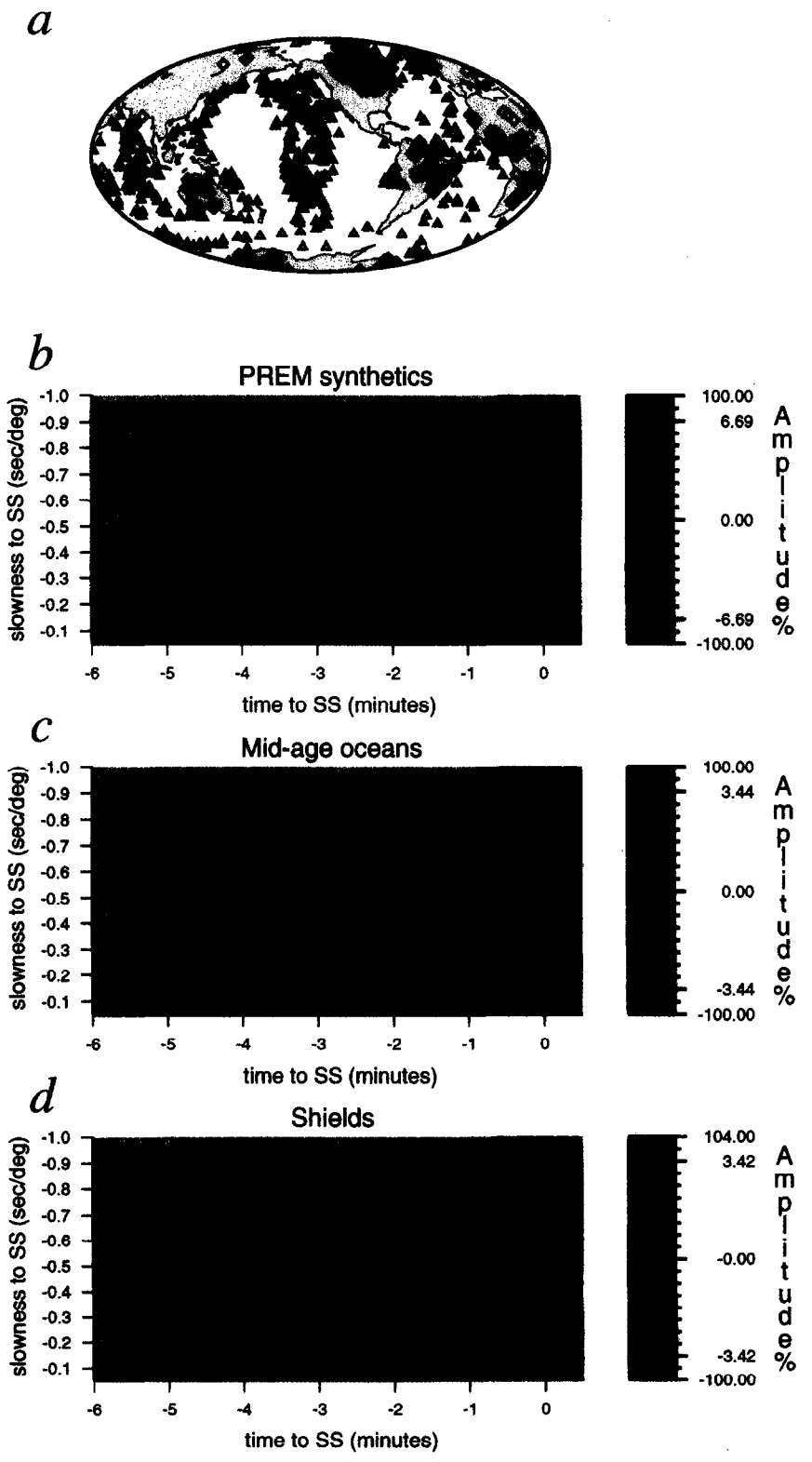
a
b
PREM synthetics
slowness to SS (sec/deg)
-1.0
-0.9
-0.8
-0.7
-0.6
-0.5
-0.4
-0.3
-0.2
-0.1
-6
-5
-4
-3
-2
-1
0
time to SS (minutes)
100.00
6.69
0.00
-6.69
-100.00
Amplitude %
c
Mid-age oceans
slowness to SS (sec/deg)
time to SS (minutes)
100.00
3.44
0.00
-3.44
-100.00
Amplitude %
d
Shields
slowness to SS (sec/deg)
time to SS (minutes)
104.00
3.42
-0.00
-3.42
-100.00
Amplitude %

influenced by the topography of the 660-km discontinuity. It is sensitive to the thermal structure and possibly chemical heterogeneities in the transition zone.

With regard to the presence of *520* beneath the oceans and its absence under shields, it is well established that the β-phase to γ-spinel transformation, corresponding to *520*, is associated with a very modest increase in density and elastic moduli [27,32,33]. This translates into a seismic velocity increase of only about 1% or about an order of magnitude less than is associated with the olivine to β-phase and γ-spinel to perovskite + magnesiowüstite transformations. In the pyrolite model, the olivine content of the mantle is 60–70%; therefore, the actual velocity increase one might expect is about 0.6–0.7%. Such an increase may be just resolvable with our reflectivity data and is represented in the feature at −3.25 min that we see in our slowness profile of the suboceanic mantle. If the olivine content drops below the pyrolite level, to 40–50% of the mantle mineralogy, it is conceivable that our seismic imaging techniques will fail to detect the corresponding 0.4–0.5% increase in velocity. If continental roots can extend into the upper mantle transition zone and are sufficiently more viscous than neighboring suboceanic mantle [34], then they may be excluded from the main mantle flow associated with ridges and trenches, thus surviving short term (200 my) recycling.

Temperature may also effect the depth of the β-phase to γ-spinel transformation and can, in principle cause it to 'disappear' under special conditions. Fig. 4 shows that the three transformations boundaries in olivine have different P–T slopes and that the β-phase to γ-spinel boundary converges with the other two and vanishes there. The phase diagram can be combined with the seismic data on discontinuity depth to estimate transition zone temperature – assuming that the mantle is homogeneous and rich in olivine component with composition Fo90. It seems unlikely, however, that either convergence can explain the absence of *520* beneath continental shields because the convergences occur at unrealistic mantle temperatures and depths – convergence with the olivine to β-phase boundary is too cold and too shallow, while convergence with γ-spinel to perovskite + magnesiowüstite is too hot and too shallow. It is conceivable that the β-phase to γ-spinel boundary is shifted just enough by the lower temperatures beneath continents to be in the interference field of the signal from *410* and hence be obscured by its proximity. It is, however, doubtful that the modest temperature perturbation of 30–40°C from the global average that we see in the *410* beneath continents is sufficient to produce this interference effect.

Difference in temperatures beneath the shields and oceans represents another possible way to explain the apparent absence of reflections from *520*. According to Bina and Wood [36] and Helffrich and Bina [37], cooler temperatures would broaden the two-phase β-phase to γ-spinel loop, decreasing the effective reflection coefficient and rendering the discontinuity less visible. However, since the tomographic models such as S12_WM13 do not display a clear correlation between the high velocity anomalies (cooler mantle) in the transition zone (Fig. 1e), and the regions where *520* signal is weak, it is more likely that the ocean-shield difference in the occurrence of *520* is a result of chemical heterogeneities in the mantle. The fact that we do not see the reflections from *520* in regions where there has been no recent

Fig. 3. Slant–stack comparison of the regional occurrence of the 520-km discontinuity under mid-age ocean and shields. (a) Data used in the regional stacking. Solid triangles = mid-age ocean reflection points (*712*); open diamonds = shield reflection points (*664*). (b) Slowness profile (in color scale) generated using stacks of synthetic seismograms in the mid-age ocean region. Red contours = positive amplitudes in the stacks; blue contours = negative amplitude in the stacks. The peak amplitude of SS is denoted by *100* on the amplitude percent scale. The percentage of S660S peak amplitude with that of SS is denoted by 6.69, and the colors below uniformly scale to 0 (yellowish green). The arrivals corresponding to S660S, S410S and S220S, as in PREM [23], are denoted by *660*, *410* and *220*, respectively; PREM [23] does not have a *520* discontinuity. The vertical location of the depth labels corresponds to the expected differential slowness. (c) Slowness profile generated using only the mid-age ocean data shown in (a). Clear arrivals corresponding to S660S, S410S are denoted; S220S is absent in the stack. The additional arrival denoted by *520* comes both at the correct slowness and travel time for a bottom side reflection from a discontinuity near the depth of 520 km. (d) Slowness profile generated using the shield data shown in (a). Only S660S and S410S are evident in the stacks. The arrival of S520S, which is present in (c), cannot be identified in this case. The figures are made using the GMT [31] mapping software.

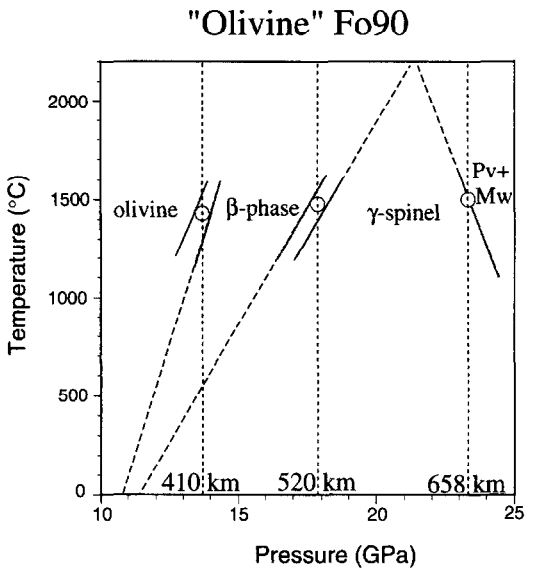

Fig. 4. Pressure versus temperature phase diagram for olivine composition with 90 mol% Mg_2SiO_4 and 10 mol% Fe_2SiO_4 (Fo90). Labeled are the stability fields for olivine, β-phase, γ-spinel, and perovskite + magnesiowüstite. The unlabeled narrow regions between the phase boundaries are the stability fields where two phases coexist at equilibrium (i.e. olivine + β-phase and β-phase + γ-spinel). The bold-line phase boundaries are from the experimental data of Katsura and Ito [27] and Ito and Takahashi [35]. The circles indicate the coincident P–T location for seismic discontinuities at 410, 520, and 658 km and phase transformations in Fo90. The dashed lines are linear extrapolations of the phase boundaries. Note that the olivine to β-phase boundary is at 410 km depth when the temperature is 1425°C, and the β-phase to γ-spinel phase boundary is at 520-km depth when the temperature is approximately 1460°C. If the temperature is significantly lower than 1460°C, then the β-phase to γ-spinel transformation occurs 'closer' to the olivine to β-phase transformation and at shallower depths. It is conceivable that this temperature effect could bring the β-phase to γ-spinel transformation 'in the shadow' of *410* and make *520* disappear beneath continental shields. Alternatively, a decrease in olivine content could make *520* disappear (see text).

subduction (Africa) argues in favor of the super-deep continental root hypothesis rather then injection of a cold material through the subduction process.

If the ocean-shield difference in the *520* reflection coefficient is real, then it has significant geophysical and geochemical implications. The weak reflections from *520* beneath continental shields may be sensitive indicators of chemical heterogeneities in the mantle; e.g. if the olivine content is lower under shields than at comparable depths beneath oceans, then the jump in acoustic impedance at *520* might be too small to produce a reflection large enough to be consistently detected. An olivine-depleted continental root extending into the transition zone could be a remnant of primordial differentiation [33] that has been excluded from the main mantle flow associated with ridges and trenches, thus surviving short term (200 My) recycling. However, this would also require that the material remained in place beneath continents.

Acknowledgements

We thank Göran Ekström, Jeroen Tromp, Wei-jia Su, Xian-feng Liu and Meredith Nettles for their help during preparation of the manuscript. We also thank Richard J. O'Connell for helpful suggestions and comments on the subject matter. Peter Shearer kindly sent us his tabulated results from an earlier study and also provided us with helpful comments. This research has been supported by grants from the National Science Foundation. ***[RO]***

References

[1] W.-J. Su, R.L. Woodward, A.M. Dziewonski, Degree 12 model of shear velocity heterogeneity in the mantle, J. Geophys. Res. 99 (1994) 6945–6980.

[2] G. Masters, S. Johnson, G. Laske, H. and Bolton, A shear-velocity model of the mantle, Phil. Trans. R. Soc. Lond. 354 (1996) 1285–1411.

[3] X.-D. Li, B. Romanowicz, Global mantle shear velocity model developed using nonlinear asymptotic coupling theory, J. Geophys. Res. 101 (1996) 22245–22272.

[4] G. Ekström, A.M. Dziewonski, Higher resolution upper mantle S velocity structure, Trans. Am. Geophys. Union Suppl. 77 (1996) F483.

[5] A.M. Dziewonski, A.M. Forte, W.-J. Su, R.L. Woodward, Seismic tomography and geodynamics, Jeffreys Vol. IUGG 16 (1993) 67–105.

[6] J. Revenaugh, T.H. Jordan, A study of mantle layering beneath the Western Pacific, J. Geophys. Res. 94 (1989) 5787–5813.

[7] J. Revenaugh, T.H. Jordan, Mantle layering from ScS reverberation: 2. the transition zone, J. Geophys. Res. 96 (1991) 19763–19780.

[8] L.P. Vinnik, R.A. Avetisjan, N.G. Mikhailova, Heterogeneities in the mantle transition zone from observations of P-to-SV converted waves, Phys. Earth Planet. Inter. 33 (1983) 149–163.

[9] G. Bock, R. Kind, A global study of S-to-P and P-to-S conversions from the upper mantle transition zone, Geophys. J. Int. 107 (1991) 117–129.
[10] P.M. Shearer, Seismic imaging of upper-mantle structure with new evidence for a 520-km discontinuity, Nature 334 (1990) 121–126.
[11] K. Stammler, R. Kind, N. Petersen, G. Kosarev, L. Vinnik, L. Qiyuan, The upper mantle discontinuities: correlated or anticorrelated, Geophys. Res. Lett. 19 (15) (1992) 1563–1566.
[12] P.M. Shearer, Global mapping of upper mantle reflectors from long-period SS precursors, Geophys. J. Int. 115 (1993) 878–904.
[13] P.M. Shearer, Transition zone velocity gradients and the 520-km discontinuity, J. Geophys. Res. 101 (1996) 3053–3066.
[14] J. Gossler, R. Kind, Seismic evidence for very deep roots of continents, Earth Planet. Sci. Lett. 138 (1996) 1–13.
[15] M.F. Flanagan, P.M. Shearer, Imaging global topography on transition zone velocity discontinuities by stacking SS precursors, Trans. Am. Geophys. Union Suppl. 77 (1996) F472.
[16] M.F. Flanagan, P.M. Shearer, Global mapping of topography on transition zone velocity discontinuities by stacking SS precursors, J. Geophys. Res., in press.
[17] P.M. Shearer, T.G. Masters, Global mapping of topography on the 660-km discontinuity, Nature 355 (1992) 791–796.
[18] G. Bock, Synthetic seismogram images of upper mantle structure: no evidence for a 520-km discontinuity, J. Geophys. Res. 99 (1994) 15843–15851.
[19] H.M. Benz, J.E. Vidale, Sharpness of upper-mantle discontinuities determined from high-frequency reflections, Nature 365 (1993) 147–150.
[20] J. Mechie, A.V. Egorkin, K. Fuchs, T. Ryberg, L. Solodilov, F. Wenzel, P-wave mantle velocity structure beneath northern Eurasia from long-range recordings along the profile Quartz, Phys. Earth Planet. Inter. 79 (1993) 269–286.
[21] A.M. Dziewonski, D.L. Anderson, Preliminary reference Earth model, Phys. Earth Planet. Inter. 25 (1981) 297–356.
[22] X.-F. Liu, J. Tromp, Uniformly valid body-wave ray theory, Geophys. J. Int. 127 (1996) 461–491.
[23] A.M. Dziewonski, F. Gilbert, The effect of small, aspherical perturbations on travel times and a re-examination of the corrections for ellipticity, Geophys. J.R. Astron. Soc. 44 (1976) 7–18.
[24] R. van der Hilst, R. Engdahl, W. Spakman, G. Nolet, Tomographic imaging of subducted lithosphere below Northwest Pacific island arcs, Nature 353 (1991) 37–43.
[25] G. Masters, T.H. Jordan, P.G. Silver, F. Gilbert, Aspherical Earth structure from fundamental spheroidal-mode data, Nature 298 (1982) 609–613.
[26] W.-J. Su, A.M. Dziewonski, Predominance of long-wavelength heterogeneity in the mantle, Nature 352 (1991) 121–126.
[27] T. Katsura, E. Ito, The system Mg_2SiO_4–Fe_2SiO_4 at high pressures and temperatures; precise determination of stabilities of olivine, modified spinel, and spinel, J. Geophys. Res. 94 (1989) 15663–15670.
[28] T.H. Jordan, The continental tectosphere, Rev. Geophys. Space Phys. 13 (1975) 1–12.
[29] T.H. Jordan, Composition and development of the continental tectosphere, Nature 274 (1978) 544–548.
[30] T.H. Jordan, Global tectonic regionalization for seismological data analysis, Bull. Seismol. Soc. Am. 71 (1981) 1131–1141.
[31] P. Wessel, W.H.F. Smith, GMT-3, 1995, 77 pp.
[32] A.E. Ringwood, Composition and Petrology of the Earth's Mantle, McGraw-Hill, New York, 1975, 618 pp.
[33] C.B. Agee, D. Walker, Olivine flotation in mantle melt, Earth Planet. Sci. Lett. 90 (1988) 144–156.
[34] M. Manga, R.J. O'Connell, The tectosphere and post glacial rebound, Geophys. Res. Lett. 22 (1995) 1949–1952.
[35] E. Ito, E.F. Takahashi, Postspinel transformations in the system Mg_2SiO_4–Fe_2SiO_4 and some geophysical implications, J. Geophys. Res. 94 (1989) 10637–10646.
[36] C.R. Bina, B.J. Wood, Olivine–spinel transitions; experimental and thermodynamic constraints and implications for the nature of the 400-km seismic discontinuity, J. Geophys. Res. 92 (1987) 4853–4866.
[37] G. Helffrich, C.R. Bina, Frequency dependence of the visibility and depths of mantle seismic discontinuities, Geophys. Res. Lett. 21 (1994) 2613–2616.